Article

Single Nanoparticle Mass Spectrometry as a High Temperature Kinetics Tool: Sublimation, Oxidation, and Emission Spectra of Hot Carbon Nanoparticles

Collin R. Howder,[†] Bryan A. Long,[†] Dieter Gerlich,[‡] Rex N. Alley,[†] and Scott L. Anderson*[,†]

[†]Department of Chemistry, University of Utah, 315 South 1400 East, Salt Lake City, Utah 84112, United States
[‡]Department of Physics, Technische Universität, 09107 Chemnitz, Germany

Ⓢ *Supporting Information*

ABSTRACT: In single nanoparticle mass spectrometry, individual charged nanoparticles (NPs) are trapped in a quadrupole ion trap and detected optically, allowing their mass, charge, and optical properties to be monitored continuously. Previous experiments of this type probed NPs that were either fluorescent or large enough to detect by light scattering. Alternatively, small NPs can be heated to temperatures where thermally excited emission is strong enough to allow detection, and this approach should provide a new tool for measurements of sublimation and surface reaction kinetics of materials at high temperatures. As an initial test, we report a study of carbon NPs in the 20−50 nm range, heated by 10.6 μm, 532 nm, or 445 nm lasers. The kinetics for sublimation and oxidation of individual carbon NPs were studied, and a model is presented for the factors that control the NP temperature, including laser heating, and cooling by sublimation, buffer gas collisions, and radiation. The estimated NP temperatures were in the 1700−2000 K range, and the NP absorption cross sections ranged from ~0.8 to 0.2% of the geometric cross sections for 532 nm and 10.6 μm excitation, respectively. Emission spectra of single NPs and small NP ensembles show a feature in the IR that appears to be the high energy tail of the thermal (blackbody-like) emission expected from hot particles but also a discrete feature peaking around 750 nm. Both the IR tail and 750 nm peak are observed for all particles and for both IR and visible laser excitation. No significant difference was observed between graphite and amorphous carbon NPs.
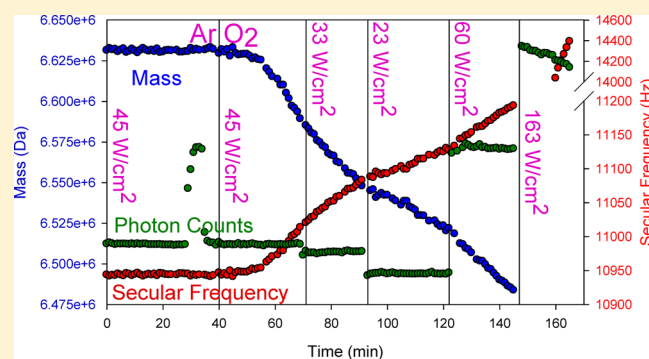
I. INTRODUCTION

There has been significant progress toward materials that can withstand temperatures well above 3000 K, important in applications such as hypersonic flight and high temperature combustion.[1] In many such applications, chemistry at the solid (or liquid)−gas interface is important, yet typical UHV surface science techniques are difficult to apply at temperatures above ~2300 K due to issues with mounting, heating, and measuring the temperature of macroscopic samples. We recently reported several studies of single CdSe/ZnS core/shell nanoparticles (NPs), levitated and laser heated in a radio frequency trap, where we were able to monitor kinetics for sublimation and oxidation, as well as the visible/near-IR emission spectra.[2−5] Although the temperatures of interest were low in those studies, the single nanoparticle mass spectrometry method appears to be a promising candidate for measurement of high temperature kinetics, complementary to other approaches such as laser-induced incandescence,[6] or aerosol methods.[7]

The approach is adapted from single particle mass spectrometry experiments first reported by Hars and Tass,[8] and developed for different applications by Gerlich et al.,[9−12] Chang et al.,[13−16] and Bieske et al.[17−20] In such experiments, a

single nanoparticle (NP) is trapped in an AC quadrupole ion trap, and the mass (M) is determined by measuring the frequency of the particle's "secular" motion in the trap, with motion detected optically. In past experiments, particles have been detected by either light scattering or laser-induced fluorescence (LIF). Here we use both visible and CO_2 laser-induced photoluminescence (PL) to track particle motion, allowing continuous measurement of the NP charge and mass, as individual NPs are heated or reacted with O_2. Measurements of PL emission spectra provide insight into the nature of the emitting states, and a model is developed of the laser heating and cooling mechanisms that determine the NP temperature. On the basis of this model, we are able to estimate the absorption cross sections for the NPs, both at 532 nm and at 10.6 μm.

Carbon was chosen for these initial experiments, partly because it absorbs strongly at the available laser wavelengths but also because there is extensive literature on carbon sublimation kinetics, due to the importance of carbon in applications such as aerodynamic heat shields and in accelerator targets.[21−27] Data exists on graphite vapor pressures over a broad temperature range, on the distribution of C_n species present in the vapor, and on rates of sublimation into a vacuum. This literature is essential, providing data for comparison with the nanoparticle results, and aiding in understanding the heating and cooling processes that determine the NP temperatures.

II. EXPERIMENTAL METHODS

The experiments used positively charged carbon NPs which were suspended in a quadrupole ion trap (Paul trap). Our instrument and NP trapping approach have been discussed in detail elsewhere.[3] Briefly, the instrument is equipped with an electrospray ionization (ESI) source and two differentially pumped ion guides to carry NPs to the trap. There is a pneumatically operated slide valve built into an ion lens between the two ion guides, which is used to isolate the trap chamber from the high flux of gas from the source, and also to gate the NP beam. Graphite NPs were prepared by milling 99.9% graphite powder (Alpha Aesar) under N_2, in a tungsten carbide-lined milling jar with tungsten carbide media, using a Retsch PM-400 planetary mill operated at 300 rpm for 6 h. For comparison, amorphous carbon NPs were prepared by milling a small piece of 1 mm thick glassy carbon plate (CH instruments) for 6 h in a SPEX 8000 mill, using tungsten carbide media and a tungsten carbide-lined jar.

To put the graphite NPs into the gas phase, they were sonicated in methanol to form a dilute suspension, and then, 0.2 mL of the suspension was mixed with 2 mL of 1 mM ammonium acetate in a syringe, just prior to injection into the ESI source, which was operated at +3 kV. The amorphous carbon NPs were simply suspended by sonication in an ∼1 mM solution of ammonium acetate in methanol. The suspensions were stable for at least several hours—much longer than the <5 min needed for a typical single particle trapping process. For the experiments discussed below, the ion guides were run at 104 kHz with amplitudes of 300−400 V, selectively transmitting species with mass/charge (M/Q) ratios in the 10^4−10^6 Da/e range, filtering out species such as molecular ions or large particles or aggregates. The size range probed in the trapping experiments was 20−50 nm. Figure S1 shows electron micrographs of the milled graphite dispersed on holey carbon at two magnifications. Particles in the >150 nm size range are easily seen, but because the contrast for carbon in electron microscopy is low, it is difficult to see particles in the ≤ ∼50 nm size range, or to deduce any structural details.

The quadrupole trap is a split-ring-electrode design similar to that reported by Gerlich and Decker.[28] In order to aid trapping, the trap chamber was filled to between 10 and 20 mTorr with Ar during NP injection. The trap was operated at trapping frequency, F, in the 40−60 kHz range, with amplitude V_0 = 200 V. The trapping potential was generated by a homemade generator with both F and V_0 stabilized, with F variable between 1 and 200 kHz and V_0 variable up to 200 V. Amplitudes up to ∼1200 V can be obtained using step-up transformers, but because each transformer pair has a limited frequency range, tunability is reduced. For the relatively light carbon NPs, high amplitudes were not needed.

Since positively charged particles were selected for these experiments, they are presumed to be charged by binding of ammonium cations. These may decompose to desorb NH_3 under particle heating, leaving the particles protonated. In any case, the surface contamination by NH_4^+ is quite low. As will be shown below, the particles selected for trapping have M/Q in the 200−2000 kDa/e range; thus, the concentration of charging ions (i.e., NH_4^+ or H^+) corresponds to no more than ∼6 × 10^{-5} per carbon atom, or <1 × 10^{-3} per surface carbon atom, assuming spherical particles. The concentration of charging species is, thus, below the sensitivity limits of tools (e.g., Auger electron spectroscopy) typically used to monitor contamination levels in surface science experiments.

Once trapped, NPs are detected optically using a single channel avalanche photodiode (APD) module (Laser Components COUNT). For particles larger than ∼50 nm, light scattering can be used; however, for the small particles of interest here, detection relies on emission via some combination of laser-excited photoluminescence and thermal ("blackbody"-like) emission. As shown below, for hot carbon NPs, both mechanisms contribute to detection. In the experiments below, the NPs were pumped at either 445 nm (5 W max, CW), 532 nm (0.5 W max, CW), or 10.6 μm using a CO_2 laser (10 W max, quasi-CW with average power controlled by duty-factor). When using either of the visible pump lasers, scattered light from trap surfaces is blocked using either a 532 nm notch filter or a 495 nm long pass color filter. So that NPs remain in the laser focus continuously, the lasers are loosely focused through the trap center, with beam waist diameters of ∼500 μm for the visible lasers and ∼600 μm for the IR laser. The visible laser beam waists were measured by monitoring the emission signal from a single trapped NP as the beam waist was translated through the trap center. For the IR laser, which is focused through the trap with a pair of paraboloidal mirrors, the waist was measured by translating a thin probe wire through the trap. On the basis of these estimates, the focal intensities typically ranged between 20 and 200 W/cm² for the visible lasers and between 100 and 1000 W/cm² for the IR laser. Because the beam waist diameters are much larger than the amplitude of driven motion (∼50 μm) required for secular frequency measurement, the laser intensity should be roughly independent of particle position.

For mass and charge measurements, it is necessary to work with one or at most a few NPs.[4] A single charged NP confined in a quadrupole trap driven at angular frequency Ω (=$2\pi F$) and amplitude V_0 has well-defined frequencies for motion in the axial and radial directions, ω_z and ω_r, respectively, which are determined by the NP mass (M) and charge (Q), as follows for the case of the axial motion.

$$\frac{M}{Q} = \frac{\sqrt{2}\,V_0}{\omega_z \Omega z_0^2} \tag{1}$$

Here, z_0 is a trap geometric parameter equal to 2.96 mm for our trap. An analogous expression exists for ω_r (=$\omega_z/2$); however, in the experiments below, we measure ω_z, hence M/Q, by axisymmetric resonant excitation. For this purpose, a low amplitude sinusoidal drive signal with frequency f_d is applied to an electrode in the trap structure, and f_d is swept over the range where the secular frequency ($f_z = \omega_z/2\pi$) is expected to lie. When $f_d = f_z$, axial motion of the NP is excited, resulting in the NP spending less time, on average, in the ∼50 × 50 μm² area which is imaged onto the APD detector, thus causing a drop in

the photon counting rate. For the experiments here, the trap was operated at background pressures in the mTorr range in order to moderate the particle temperature,[5] which has the additional effect of collisionally damping the NP motion on an ~0.1 s time scale, such that an intensity dip is observed as f_d is scanned through f_z. This feature is fit to a Gaussian, the center of which is taken to be the value of f_z.

To determine M, it is necessary to extract the value of Q, which is done by observing the step-like changes in the secular frequency when Q changes by ±e. In previous papers,[2−5] we used a weak electric discharge to create electrons, Ar$^+$ and Ar metastables which occasionally collided with the NP, inducing charge steps. For the present experiment, the instrument was augmented by a windowless capillary discharge vacuum ultraviolet (VUV) lamp that emits Ar I photons (11.6 and 11.8 eV), as well as some electrons and Ar metastables.[29] The lamp is mounted on a tilt stage, so that the intensity entering the trap can be adjusted by misalignment of the lamp and trap axes. The lamp is equipped with a pneumatically operated flag at the second differential pumping stage, so that short pulses of radiation can be allowed into the trap, with the pulse length adjusted so that the probability of a charge step is ~25% *per* pulse, with only an occasional step of more than ±e. By measuring the frequency step height, Δf_z, corresponding to ΔQ = ±e, we determine Q from the relation: $Q/e = f_z/\Delta f_z$. Once Q is determined, the lamp is turned off; however, there are still occasional spontaneous charge steps due to collisions with stray electrons or ions in the chamber background, and thermionic electron emission can become significant as NPs are heated. When charge steps are observed in the figures below, the values of Q are indicated as integers at each step.

To investigate the processes giving rise to the detected photons, we measured low resolution emission spectra for both single NPs and small ensembles containing tens of NPs. To collect a spectrum, the emitted light was passed through a sequence of long pass filters, integrating the photon counts for times ranging from ~10 to 100 s for each filter. Emission spectra are then obtained from the difference in integrated intensities measured for successive filters. Our APD is sensitive between 400 and 1100 nm, and we used 6−10 filters to break this up into spectral regions with widths between 20 and 100 nm. To correct for background from APD dark counts and scattered laser light, we used a set of filtered photon counting data taken under identical conditions but with no NPs in the trap. The filter approach works well under low light conditions, and allows us to monitor M and Q during the spectral measurements; however, the resolution is low and the process takes ~10−15 min, so that it can only be done under conditions where the NPs are stable over that time scale.

III. RESULTS

A. Mass, Charge, and Thermal Stability of Single Carbon NPs. Figure 1 shows a typical experiment in which the axial secular frequency ($f_z = \omega_z/2\pi$) and the detected photoluminescence (PL) intensity were monitored continuously over time, while a single graphite NP was pumped at 532 nm at 46 W/cm^2, with 9 mTorr of argon buffer gas used to moderate the NP temperature. From the initial value of f_z, eq 1 can be used to calculate that the initial M/Q for this NP was 317 kDa/e. Prior to the beginning of the data record shown in the figure, the VUV lamp had been used to determine that the initial charge state was +46 e, and thus the initial mass was ~14.6 MDa, equivalent to a 27.5 nm diameter spherical particle
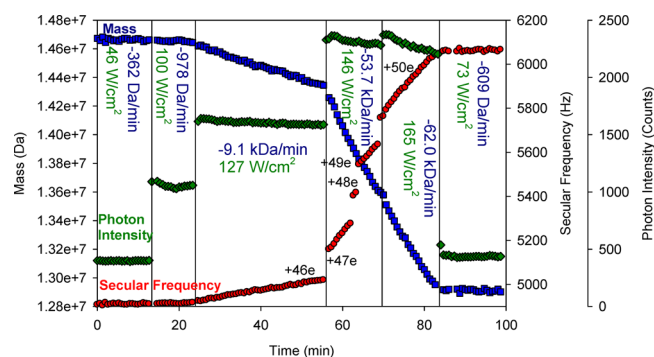

Figure 1. Secular frequency, mass, and photon intensity vs time for a single graphite NP excited at 532 nm at the intensity levels indicated. For each laser intensity, the mass loss rate is indicated in Da/min.

with bulk graphite density. After shutting off the VUV lamp at time zero, f_z (hence M) was monitored for ~15 min to establish a baseline mass loss rate, and then, the laser intensity was turned up in a series of steps, resulting in immediate increases in PL intensity. At 127 W/cm^2, the secular frequency began to increase at an obvious rate, indicating a substantial mass loss rate. At 146 W/cm^2, the mass loss rate accelerated, and there were also four charge steps, visible as discontinuities in the secular frequency record. These steps, all corresponding to an increase of Q by e, are attributed to thermionic emission of single electrons from the hot carbon particle. Because increasing Q increases the work function of the NP, and additional cooling mechanisms begin to compensate for higher pump laser intensity (see below), thermionic emission from NPs tends to be self-limiting.[2]

14.6 MDa is ~1.2 million carbon atoms, and the 362 Da/min initial mass loss rate corresponds to only about one carbon atom every 2 s, giving some idea of the sensitivity of the single nanoparticle mass spectrometric method. The mass loss rates associated with each laser power, indicated in the figure, began to increase rapidly for laser intensities of 127 W/cm^2 and above, and it can be seen that when the power was dropped back to 73 W/cm^2 at the end of the experiment, the mass loss rate also dropped to a value consistent with the low heating intensity. The mass loss rates are roughly exponentially dependent on laser intensity, as might be expected for exponential dependence of the sublimation rate on NP temperature. The laser intensity−sublimation rate relationship is complicated, however, because NP temperature depends on a number of factors besides laser intensity (see below), and the sublimation energy is likely to evolve as mass is lost from the NPs, because the distribution of basal plane, edge, and defect sites will tend to evolve as the particle loses mass. An example of the latter effect is presented below.

The relationship between detected photon signal and excitation laser intensity (I) is also interesting. For laser intensities up through 146 W/cm^2, the detected photon intensity increased approximately like $I^{1.7}$; i.e., the emission is superlinear in laser intensity but with nonlinearity that is weaker than might be expected if emission were entirely thermal ("blackbody"-like). This point is discussed further, after the emission spectral results are presented. When the pump intensity was increased to 165 W/cm^2, the photon emission did not increase as expected, and dropped noticeably during the period of high pump intensity. A number of effects could be responsible, including particle cooling by sublimation, anneal-

ing of the particle to more compact shape, loss of emissive surface states, and reduction of the absorption cross section.

We also examined thermal stability and mass loss for a single carbon NP heated using only 10.6 μm radiation from the CO_2 laser, and the results are summarized in Figure 2. The primary
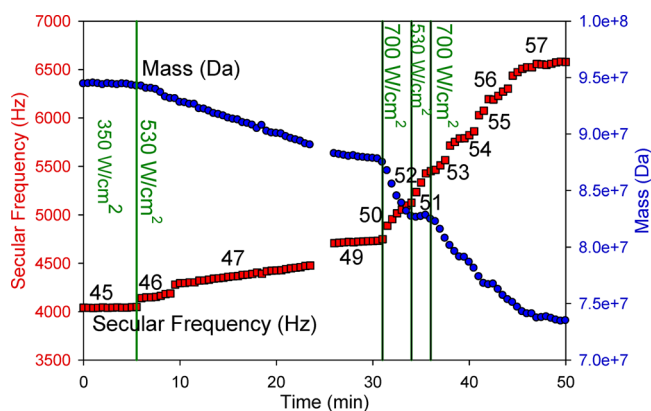

Figure 2. Secular frequency and mass for a single graphite NP as a function of time as it was pumped by a duty-factor modulated quasi-CW CO_2 laser at the intensities indicated.

motivation for using both visible and IR pump lasers was to see if there might be any obvious wavelength dependence of the excitation efficiency or thermal behavior of the carbon particles. According to Mie theory,[30] the cross section for absorption and emission of light by NPs with dimensions less than the wavelength (λ) should vary approximately like λ^{-1}. Thus, for NPs in the ≤50 nm range, we expect that the CO_2 laser should be absorbed ~20 times less efficiently than the 532 nm laser. It is difficult to compare absorption efficiency quantitatively because the CO_2 laser is duty factor modulated; however, the results in Figure 2 show that substantially higher average IR laser intensities are required to drive the same rate of carbon sublimation, compared to excitation at 532 nm. The dependence of the emission spectra on pump wavelength is discussed below.

The NP in Figure 2 had an initial mass of 94.5 MDa, equivalent to an ~51.5 nm diameter spherical particle with graphite density. Steps in the secular frequency were observed as soon as the laser intensity was increased to 530 W/cm², and the Q values are indicated as integers on the steps. Note that the mass was nearly constant for 350 W/cm² intensity and then decreased with increasing slope as the laser intensity was increased, with ~22% total mass loss over the course of the experiment. For an average laser intensity of 530 W/cm², the mass loss rate was 293 kDa/min (~24 400 C atoms/min), increasing to 1.65 MDa/min (~138 000 C atoms/min) for 700 W/cm². The nonlinear increase in mass loss rate reflects the expected exponential dependence of the sublimation rate on NP temperature. For a few minutes during the high power phase of the experiment, the IR laser intensity was decreased back to 530 W/cm², and it can be seen that M actually increased slightly, presumably due to reaction of the clean particle surface with species in the chamber background.

When 700 W/cm² heating was resumed, the mass loss rate was nearly identical to the rate during the first 700 W/cm² period but then gradually decreased. A similar, though less obvious, slowing of the mass loss rate is also apparent at the end of the first 530 W/cm² heating phase. Careful examination of Figure 1 shows analogous but much weaker curvature in the

mass record during the 146 and 165 W/cm² heating phases. From these preliminary experiments, it is not possible to say with certainty why the mass loss rates slow with time; however, it is likely that this reflects preferential desorption of carbon from less stable surface sites (defects, basal plane edges), where the desorption energy is lower. As a result, we expect that the distribution of sublimation energies should evolve to higher average energy as mass is lost, slowing the mass loss rate. Note that the 22% overall mass loss in Figure 2 corresponds to an ~4 nm diameter reduction for the equivalent spherical NP; thus, it is clear that at least several monolayers of carbon were lost. There may also have been a reduction in absorption cross section as the NP lost mass; however, it seems unlikely that the decrease could be fast enough to account for the slowing mass loss.

B. Oxidation Chemistry of Trapped Graphite NPs. We made a preliminary study of the oxidation chemistry of single trapped graphite NPs. One example experiment is shown in Figure 3. A single graphite NP of initial mass ~6.63 MDa,
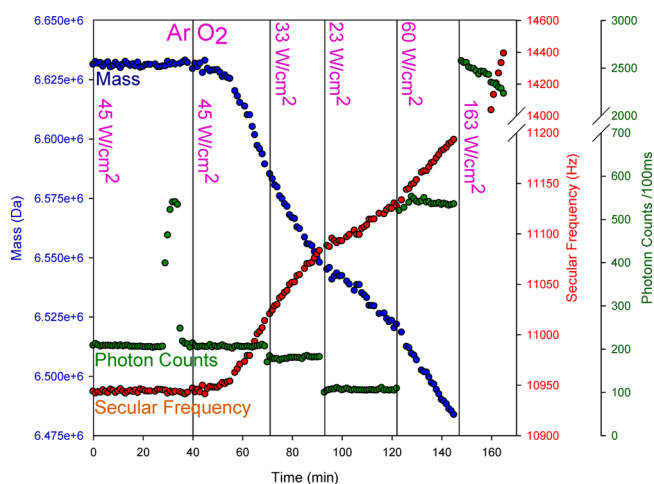

Figure 3. Secular frequency, photon intensity, and mass as a function of time for a single graphite NP pumped at 532 nm at the indicated intensities, in either argon or O_2 gases at 1 mTorr pressure.

equivalent to a 21.2 nm diameter spherical particle, was trapped and pumped at 532 nm (45 W/cm²), with 1 mTorr of argon buffer gas, resulting in sufficient emission for particle tracking, but little sublimation, as might be expected from Figure 1. M and Q were measured using charge steps prior to the start of the data record shown in the figure. At ~30 min, the pump laser was turned up to ~61 W/cm² for a few minutes, resulting in higher PL signal but no significant mass loss, again consistent with Figure 1. During this initial ~40 min period with the NP trapped with argon buffer gas, the average mass loss rate was ~25 Da/min; i.e., the particle lost only ~83 of the initial 5.53 × 10⁵ atoms. Because the maximum laser intensity during this experiment was only 60 W/cm², we can reasonably assume that the carbon sublimation rate remained small throughout.

At 40 min, the argon was replaced with O_2 at the same 1 mTorr pressure, keeping the excitation laser intensity constant. This resulted in a factor of 100 increase in mass loss rate, to ~2.38 kDa/min (~200 carbon atoms/min), presumably due to oxidation reactions forming CO_2 or CO. Recent work of Murray et al.[31] suggests that CO should dominate; however, because our method directly measures the mass loss rate, our kinetic analysis does not depend on the product identity.

Subsequently, the laser intensity was varied, and as might be expected, the mass loss rate and PL intensity varied as well. At the end of the experiment, the laser intensity was increased to 163 W/cm², and under those conditions, the secular frequency changed so rapidly (note scale change) that the program used to automatically follow the secular frequency over time temporarily lost track. Because charge steps may have occurred during this time, the value of Q at the end of the experiment was unknown, and therefore, M was also undetermined in the final heating stage. See below for our approach to this problem.

There are several points of interest regarding the oxidation experiment. As noted, the mass loss rates are much higher in O_2 than in argon; thus, carbon sublimation can be neglected to a good approximation. The NP oxidation kinetics are clearly not simple, however. For example, the oxidative mass loss rate has a complex dependence on pump laser intensity. At an initial intensity of 45 W/cm², the mass loss rate was 2.38 kDa/min, and the rate decreased monotonically as the laser intensity was decreased, to 1.85 kDa/min at 33 W/cm² and 0.915 kDa/min at 23 W/cm². However, when the intensity was subsequently increased to 60 W/cm², the mass loss rate only increased to 1.66 kDa/min—slower than the rate observed at 33 W/cm².

For fixed O_2 pressure, the rate of oxidative mass loss is expected to depend on NP temperature and the availability of reactive sites on the NP surface. The temperature is set by the balance between heating by laser absorption and surface oxidation reactions and cooling by collisions, photon emission, and carbon sublimation. As shown below, the NP temperature is not linear in laser intensity; however, in the absence of large changes in NP size and optical properties, temperature does increase with increasing laser intensity. In this case, the mass changed by only 3% over the course of the experiment; thus, we would not expect significant changes in the absorption cross section at 532 nm. Consistent with this expectation, the PL signal was found to be roughly linear with laser intensity up to 45 W/cm², suggesting that the absorption cross section was roughly constant. At higher laser intensities, the PL signal increased nonlinearly, but as discussed below, superlinear dependence of PL signal on laser intensity is not unexpected because, at high NP temperatures, there is evidence for thermal photon emission, and also thermal population of excitonic and surface states.

It appears, therefore, that the slowing of oxidative mass loss rate over time implies that the NP surface had a diminishing number of reactive sites. This is not just a matter of reduced NP surface area, because the mass loss was only ~3%. Instead, we propose that the oxidation reactions occur primarily at defect sites on the graphite NP surface, and that these are selectively lost to some combination of annealing and reaction with O_2. Given the structure of graphite, these reactive sites are likely to be exposed edges of graphite basal planes, or local defects generated by milling. The slowing in oxidation rate is, therefore, essentially due to the same mechanism invoked above to rationalize the slowing of sublimation rates over time.

The time dependence of the onset of oxidation when the Ar was replaced by O_2 at the 40 min mark in Figure 3 is also interesting. The gas composition and temperature stabilize within seconds after such a change, but it can be seen that it took over 10 min for the mass loss to accelerate to a stable rate. This acceleration cannot be related to any NP temperature increase due to the oxidation reaction, because oxidative mass loss rate corresponds to only ~200 C atoms/min, and the exothermicity associated with CO or CO_2 formation is

negligible compared to the laser heating rate, as discussed below.

We propose the following rationalization for the oxidation induction period. The NPs were introduced into the trap from solution, and then spent 40 min in the trap prior to O_2 introduction. The argon buffer gas used is 99.995% pure; however, after a series of electrospray experiments, the vacuum chamber has a base pressure of ~10^{-7} Torr, which certainly includes methanol and other organic species. It is not unreasonable to assume, therefore, that defect sites on the NPs are initially partially passivated by adsorption/reaction of species either in solution or in the vacuum system, with some steady state coverage determined by the NP temperature and background concentrations of passivating species. When the gas was switched to O_2, the initial number of sites capable of reacting with O_2 was apparently low, but as reaction proceeded, additional sites became available and eventually a new steady state site density was established.

Figure 4 shows another example of oxidation chemistry, where the oxidation rate was varied by varying the O_2 pressure,
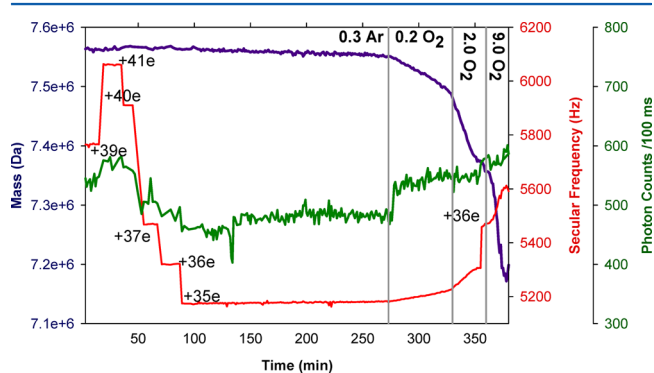

Figure 4. Secular frequency, photon intensity, and mass as a function of time for a single graphite NP pumped at 532 nm in either 0.3 mTorr of argon, or between 0.2 mTorr and 9 mTorr of O_2.

rather than the pump laser intensity. A single graphite NP was trapped, and M and Q were determined from the secular frequency during a series of charge steps. In this example, we show the charge steps to make the point that the PL signal is somewhat charge dependent, roughly tracking the changes in f_z. As discussed elsewhere, higher charge states result in tighter confinement of the NP, with concomitant increase in PL collection efficiency.[2] This NP had an initial M value of 7.56 MDa, equivalent to a 22 nm spherical NP with bulk graphite density. For the first 4.5 h, the NP was trapped in 0.3 mTorr of argon and pumped at 532 nm with an intensity of 39 W/cm² to establish a baseline. Under these conditions, the NP lost mass at a roughly constant rate of ~77 Da/min (6.4 C atoms/min).

At 270 min, the argon atmosphere was switched to O_2 at a pressure of 0.2 mTorr, resulting in an increase of the mass loss rate to 1.10 kDa/min (~92 C atoms/min). Note that the induction period is much less obvious in this experiment, compared to that in Figure 3, which we attribute to the lower gas pressures used. Even for a reactive gas like O_2, the dominant effect is actually collisional cooling of the laser-heated NPs; thus, lower pressure equates to higher NP temperature, which presumably decreased the passivation of reactive sites. That the NP temperature was higher than in Figure 3 is shown by the higher initial mass loss rate by sublimation during initial trapping in Ar. One interesting observation in this experiment
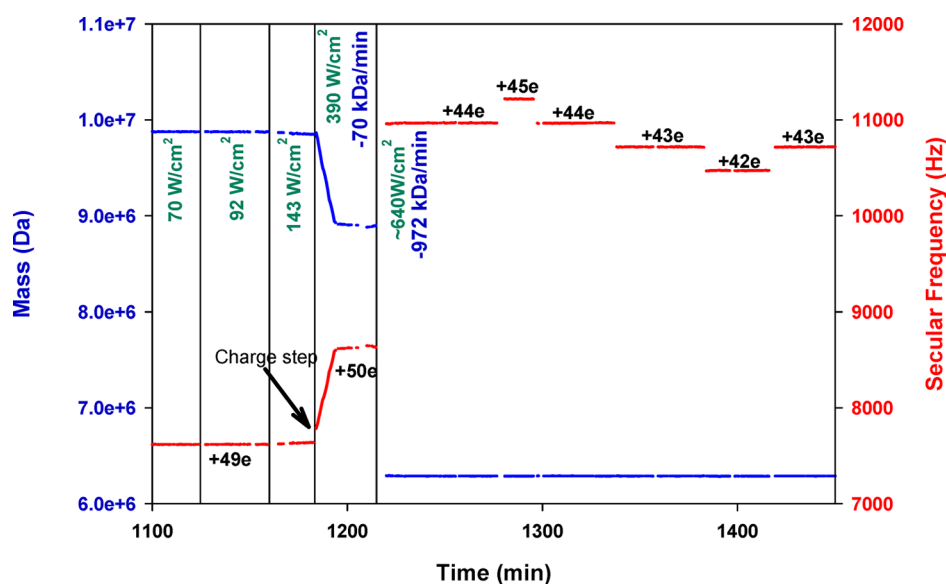
Figure 5. Measurement of very rapid (972 kDa/min) mass loss from a single graphite NP under high intensity laser irradiation.

was that the PL signal jumped ~10% when the atmosphere was changed to O_2, and then increased slowly for the duration of the experiment. No such increase was observed in the first oxidation experiment shown in Figure 3.

At 330 min, the O_2 pressure was increased to 2 mTorr, resulting in an increase in the rate of mass loss to 4.78 kDa/min (399 C atoms/min), and finally, the O_2 pressure was increased to 9 mTorr, resulting in a mass loss rate of 12.71 kDa/min (1060 C atoms/min). In this case, the mass loss rate at the two higher pressures is roughly linear in O_2 pressure, suggesting that the number of reactive sites on the NP surface was roughly constant under those conditions. At 0.2 mTorr, however, the mass loss rate was only about half of that predicted by linear extrapolation from the higher pressure experiments, suggesting that the number of active sites was also about half. This observation is reminiscent of the induction period observed in the first oxidation experiment, and suggests that, for low laser intensities and/or low O_2 pressures, the oxidation rate is not high enough to keep the NP surface clean and active. Analysis of variable pressure experiments like this is complicated by the fact that, particularly at the higher pressures, collisional cooling starts to have a significant effect on the NP temperature. See below for more discussion of thermal issues in these experiments.

C. Measuring Mass Loss Rates Too Fast for Secular Frequency Tracking. As shown in Figure 3, it is possible that for high heating rates, especially under reactive conditions, the secular frequency may change so rapidly that the data acquisition program is not able to track the changes. Of course, it is trivial to re-establish tracking, thus redetermining M/Q; however, the final M is unknown because it cannot be excluded that charge steps occurred during the untracked period. In that case, we simply remeasure M and Q at the end of the experiment, using the VUV lamp to induce a set of charge steps.

An example of that procedure is shown in Figure 5, where M (9.87 MDa) and Q (49) were determined for a single carbon NP, while pumping at 532 nm with 40 W/cm^2 intensity, in 3 × 10^{-4} Torr of Ar buffer gas. After allowing the NP to sit overnight under 532 nm irradiation, the 532 nm intensity was changed to 70, 92, and 143 W/cm^2, resulting in only modest

mass loss. At 1180 min, the 532 nm intensity was decreased to 84 W/cm^2 and left at this power for the duration of the experiment. The CO_2 laser was turned on to bring the total radiation intensity to 390 W/cm^2, which drove mass loss of 910 kDa over the course of ~13 min, giving a mass loss rate of ~70 kDa/min. Note the appearance of a single charge step at the beginning of this heating period.

At 1212 min, the CO_2 laser was turned up to give a total radiation intensity of ~640 W/cm^2, which drove a large jump in secular frequency, leading to loss of tracking, shown as discontinuities in the frequency and mass records. After 160 s, the CO_2 laser was blocked, leading to a stable secular frequency, indicating a change in M/Q during the rapid heating interval of ~27%, due to some unknown combination of mass loss and charge changes. The VUV lamp was then used to induce a series of charge steps, revealing that the final charge (at the end of the rapid heating interval) was +44e; i.e., the particle had lost 6 charges. The mass was, thus, shown to have dropped by 2.59 MDa (26.2%) during the 160 s heating period, giving a mass loss rate of 16.2 kDa/s = 972 kDa/min. One interesting point in this figure is that the NP became less positively charged during the rapid heating phase. Typically, under conditions where we can still track the secular frequency, we tend to observe NPs becoming more positive at high temperatures, which we attribute to thermionic emission of electrons (see Figures 1 and 2). In this case, during the very rapid mass loss (1350 C atoms/s), it appears that there must have been emission of C_n^+, more than compensating for any electron loss.

D. Emission Properties of Trapped Graphite NPs. Emission spectra were acquired for both graphite and amorphous carbon NPs excited at 532 nm, 445 nm, and 10.6 μm. The primary questions of interest are whether the gross emission behavior varies significantly with excitation wavelength, or from NP to NP. Within the limitations of the crude and slow filter-based spectral method, the answer to both questions appears to be "no". Under the conditions of these measurements (laser intensity, Ar pressure), the sublimation rates should have been slow, such that the particle sizes were approximately constant. We cannot rule out, however, the possibility that the spectral properties might have changed

during the 10−15 min acquisition time. As discussed above, for example, annealing or slow sublimation might have changed the number or type of under-coordinated defect sites, with possible effects on emission properties.

Figure 6 gives emission spectra from several ensembles of graphite NPs, with the filter cutoff wavelengths indicated by
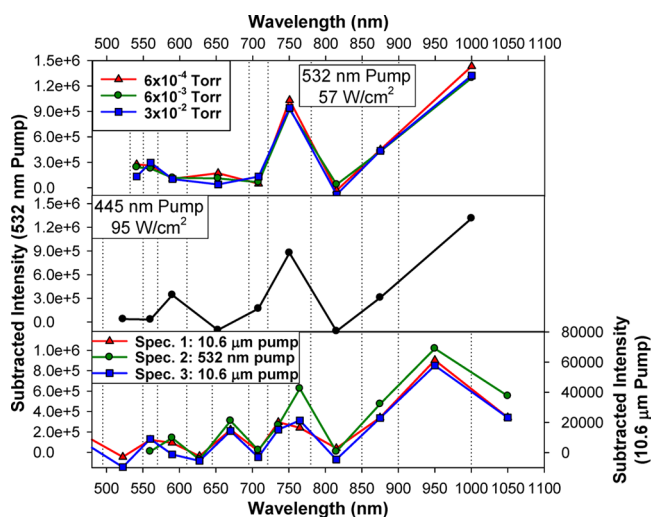

Figure 6. Emission spectra of small NP ensembles pumped at different wavelengths with different Ar buffer gas pressures. Spectra are corrected for the APD quantum efficiency vs wavelength. See Figure S1 for uncorrected spectra.

vertical dotted lines. The spectra have been corrected for the APD quantum efficiency vs wavelength, taken from manufacturer data provided with the APD. The quantum efficiency is ~54% at 500 nm, peaks at ~73% at 670 nm, and then drops to only 6% at 1100 nm. For comparison, the uncorrected spectra are given in Figure S2, showing the contribution each wavelength range makes to the raw PL count rate measured during the mass loss experiments. The main effect of the correction is to increase the spectral intensity in the near IR range. Note that Mie theory also predicts that the emissivity should vary like $\sim \lambda^{-1}$. The spectra are not corrected for this effect, but if they were, the result would be a small further enhancement in the near IR portion of the spectra.

The top frame of the figure presents emission spectra for an ensemble of graphite NPs pumped at 532 nm at 57 W/cm^2, with three different argon buffer gas pressures. The particle temperature is determined by the balance between laser heating and cooling by a combination of radiation, sublimation, and collisions with argon buffer gas. Therefore, when the pressure is decreased, keeping the laser power constant, we expect that the NP temperature should rise. The results in Figure 6 show that, for the modest range of conditions where the NPs are stable on the spectral acquisition time scale, the emission intensity and spectra do not depend strongly on pressure.

For comparison, the middle panel of the figure shows the emission spectrum for another graphite NP ensemble, pumped at 445 nm at 95 W/cm^2 with 10^{-3} Torr of Ar buffer gas present. Finally, in the bottom frame of the figure, emission spectra for a third ensemble of graphite NPs are shown. This ensemble was first pumped at 10.6 μm with ~100 W/cm^2 of average power, then pumped at 532 nm with 44.5 W/cm^2 power, and then again pumped at 10.6 μm with ~100 W/cm^2 of average power. For this set of spectra, several additional filters were used, providing additional resolution in the region around 750 nm, and an additional filter with 1000 nm cutoff wavelength was used to allow measurement of the intensity between 1000 nm and the 1100 nm APD cutoff wavelength. Note that, because the APD quantum efficiency is small (~6%) in the 1000−1100 nm range, the correction for APD sensitivity is large; thus, the uncertainty for this last spectral data point is also large. For this reason, we do not attach much significance to the apparent drop in intensity above 1000 nm.

Even as plotted, all the ensemble emission spectra appear rather similar; however, the extra filters used in some of the spectra make it difficult to compare the spectra directly. Therefore, in Figure S3, we replot all the spectra together, with the extra points present in some of the spectra added to neighboring points, so that all the spectra have identical resolution. Different absolute scales have been used for the 532 nm and 10.6 μm spectra, but this may simply reflect differences in the number of NPs present in each ensemble. The spectra really are all nearly identical, with one intense feature peaking around 750 nm and another with intensity rising toward the detector cutoff at 1100 nm. There is also weak, structureless emission in the 530−700 nm range. The spectra are clearly not very sensitive to pump wavelength, with the exception that, for 10.6 μm pumping, the intensity of the 750 nm feature is
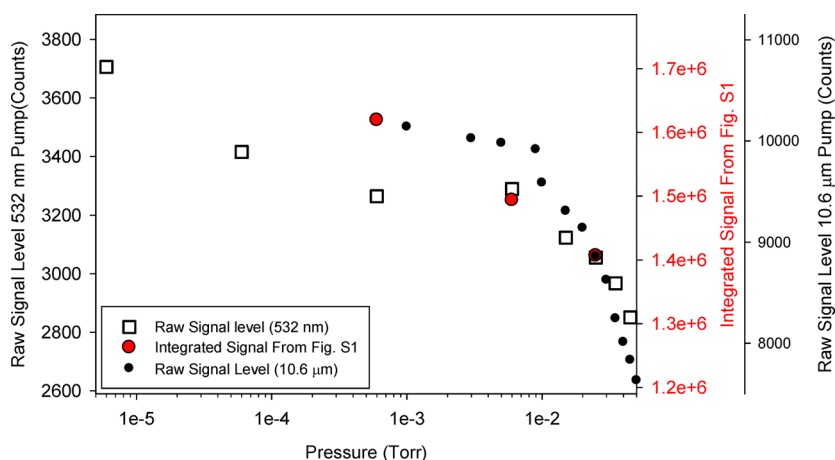

Figure 7. Total photon counts in the 530−1100 nm range as a function of Ar buffer gas pressure.

consistently ~20% lower, relative to the near-IR feature, than it is for pumping at 532 and 445 nm.

Figure 7 shows the results of three experiments where ensembles of NPs were trapped, pumped at either 532 nm or 10.6 μm at constant intensities of 41 and 100 W/cm^2, respectively, and then monitored while the argon pressure was varied. As noted above, as pressure is lowered, the NP temperature should increase, raising the possibility that the NPs might begin to sublime rapidly at low pressures. Therefore, in the first experiment, we simply measured the raw emission intensity as the pressure was dropped in steps from 4.5×10^{-2} to 6×10^{-6} Torr, rather than taking the time to measure emission spectra. As shown in Figure S2, the raw APD signal is dominated (~43%) by a signal from the feature around 750 nm, with ~23 and 34%, respectively, coming from the wavelength ranges above 800 nm and below 700 nm. For comparison, the second experimental series shown is taken from the 532 nm emission spectral measurements in the top frame of Figure S2 (uncorrected for APD sensitivity), integrated to give the total emission intensities. Finally, a third NP ensemble was pumped with 100 W/cm^2 of 10.6 μm radiation as the Ar pressure was slowly scanned from $\sim 5 \times 10^{-2}$ Torr to below 10^{-5} Torr, similar to the first experiment. Because different NP ensembles, pump lasers, and acquisition times were used, the absolute signal levels in the three experiments are quite different. To allow direct comparison, the intensity scales for the three experiments have been adjusted to align the points at 2.5×10^{-2} Torr (the highest pressure that all three data series have in common), keeping the relative range identical for each data series (scale max = 1.5·scale min).

Consider the two experiments in which emission intensity was measured as the pressure was dropped, while exciting the NPs at either 532 nm or 10.6 μm (open squares and black circles). In both, the emission intensity rose by 15−20% as the pressure was dropped from 4.5×10^{-2} to 6×10^{-3} Torr, but there was little additional increase as the pressure dropped to 6×10^{-4} Torr. For 532 nm excitation, there was a further ~14% increase in emission as the pressure was dropped to 6×10^{-5} Torr. For 10.6 μm excitation, the data series stopped at 1×10^{-3} Torr because the single NP emission intensity became very unstable, possibly because of rapid NP sublimation or thermionic electron emission. The pressure dependence of the integrated spectra (red circles) differs somewhat from those measured in the two pressure scan experiments, possibly because different ensembles were used in each experiment. It is more likely, however, that the differences result from the much slower time scale of the spectral measurements, which would have led to larger changes in the NP size distributions particularly in the lower pressure range.

The ensemble emission spectra all show multiple features, and one possible interpretation is that the features reflect the heterogeneity of the trapped NP ensembles, i.e., that the various emission features originate from different NPs in the ensembles. To test this possibility, we measured emission spectra for a number of individual graphite and amorphous carbon NPs, using the same procedure, with Q and M also determined in all but one case. Figure 8 shows emission spectra taken for different NPs, covering a significant range of both M and Q, with one NP pumped at both 532 nm and 10.6 μm. For most of the single NP spectra, the expanded filter set used in the bottom frame of Figure 6 was used, with the same considerations discussed above. It is clear that, within the signal-to-noise level of the single NP spectra, they are all quite
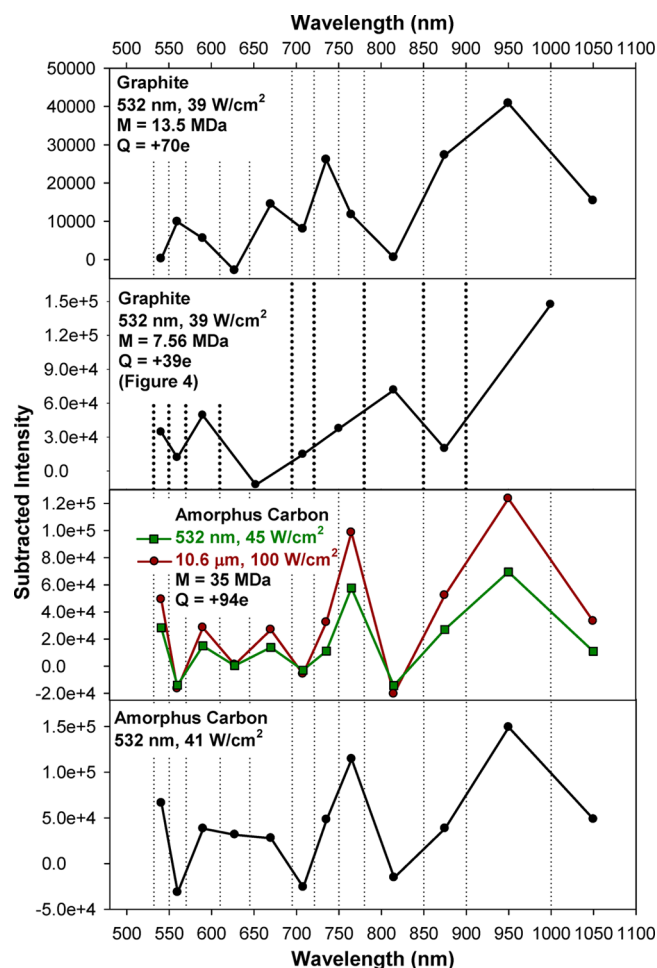

Figure 8. Emission spectra for individual carbon nanoparticles, under the conditions shown.

similar, and that they are also similar to the ensemble spectra in Figure 6. This implies that individual NPs support the full range of emission features, including the feature near 750 nm, the near-IR emission at $\lambda > 800$ nm, and weak visible emission between 530 and 700 nm.

Given that the particles are hot, it is not surprising that they might emit in the near-IR due to thermal (blackbody-like) emission; however, the intense emission peak near 750 nm, observed under both visible and IR pumping for all particles, suggests the presence of some chromophores with well-defined emission properties that are independent of particle size, crystallinity, charge, and excitation wavelength. It might be thought that some C$_n$ species subliming from the NPs could be responsible; however, the sublimation rates under the conditions used for spectral measurements are far too low to generate a detectable concentration of any gas-phase C$_n$ species.

M for the particles is equivalent to that of spherical particles in the 20−50 nm diameter range; however, the particles are likely to contain domains that are significantly smaller, due to defects introduced in the fracturing and cold-welded processes that occur during milling.[32−36] In both graphite and glassy carbon, the majority of the atoms are sp^2-hybridized, but defects and sp^3 hybridization create sp^2-hybridized domains in which the π electrons become localized. If these domains are below ~20 nm in diameter, they have significant band gaps,[24] and electron−hole recombination can lead to laser-induced

photoluminescence (PL). For example, PL has been observed in disordered carbon thin films and particles containing a mixture of sp^2- and sp^3-hybridized carbon.[37,38] Carbon NPs have received some recent attention as nontoxic alternatives to semiconductor quantum dots for photochemical and bioimaging applications. The simplest of these are individual graphene or graphene oxide sheets, which are essentially isolated sp^2-hybridized domains. The band gap and therefore the emission properties of graphene sheets depend on the size of the sp^2-hybridized domains, and certain edge effects such as oxidation and surface state passivation.[22,24,25,37,39] Graphene oxide samples with emission maxima across the visible have been synthesized, with broad emission features, spanning 100 nm or more.[22,25,39,40] Small three-dimensional carbon nanoparticles can also be luminescent, and it appears that in these systems the luminescence is a mixture of electron hole pair recombination across a band gap and PL from surface states.[24,41,42] Because our particles are likely to be quite defective, the presence of surface states that may give PL is quite likely. Such surface states could be on the outer surfaces of the NPs, or at interfaces between cold-welded subparticles.

We tentatively assign the observed emission spectral features as follows. The near-IR emission growing at long wavelengths is likely to be the tail of a thermal (blackbody-like) emission feature, most of which lies above the APD cutoff wavelength. The structured emission around 750 nm and the weak signal in the 500−700 nm range is found to be nearly identical over a range of laser pump powers and reasonably consistent from NP to NP. We attribute this signal to a combination of excitonic emission in localized sp^2-hybridized domains and emission from surface states. One point of interest is that the emission from these carbon NPs is substantially brighter than what we have seen for 5−7 nm CdSe/ZnS quantum dots in the gas phase, under similar conditions.[5] For the quantum dots, excitation at 532 nm with 100 W/cm^2 might result in PL count rates of 500−800 per second. For the carbon NPs, excitation at 532 nm with 40−60 W/cm^2 results in 2000−3000 photon counts/s; i.e., the emission is nearly an order of magnitude brighter, normalized for pump intensity.

Another point of interest is that the emission feature around 750 nm ($\approx$1.65 eV) is observed with only slightly lower intensity (Figure S2) when carbon NPs are excited at 10.6 μm, compared to excitation in the visible. This feature is attributed to relaxation of some electronic excitation, and it is not surprising that it should have high intensity when excited by radiation at 532 or 445 nm. On the other hand, it is clear that 10.6 μm radiation must be exciting phonons in the NPs, and the fact that there is still substantial emission at 750 nm implies that conversion of phonons to electronic excitation must be reasonably efficient for these carbon NPs. This effect was not seen for CdSe/ZnS core/shell quantum dots under similar conditions.[5] In that case, 10.6 μm excitation produced only weak emission near 1 μm, consistent with being the high energy tail of a thermal (blackbody-like) emission feature peaking further in the IR.

The observation that PL intensity increased under oxidizing conditions, at least for the NP in Figure 4, raised the question of whether the emission spectrum might also change, and we tested this point via the experiment shown in Figure 9. A small ensemble of graphite NPs ($\sim$3 NPs) was trapped while pumping at 32 W/cm^2 at 532 nm. Spectrum 1 was collected for the as-trapped ensemble in argon at 3×10^{-4} Torr. The atmosphere was then changed to 3×10^{-4} Torr of O_2, and
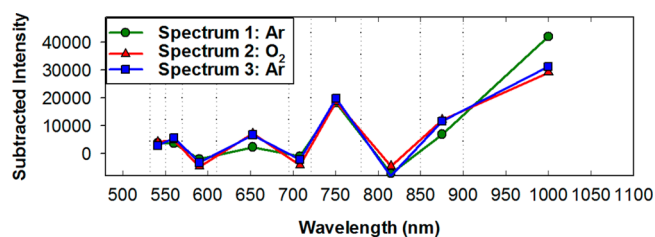

Figure 9. Comparison of spectra of a small graphite NP ensemble, pumped at 532 nm, in either Ar or O_2 gas, under conditions where slow oxidation occurs in O_2.

spectrum 2 was recorded. Finally, the atmosphere was switched back to 3×10^{-4} Torr of argon, and spectrum 3 was recorded. Note that the conditions in this experiment are such that we expect that the particles were undergoing significant oxidative mass loss during the measurement of spectrum 2. Evidently, ongoing oxidation does not have any dramatic effect on the emission spectrum or intensity, at least at this relatively low excitation laser intensity.

IV. DISCUSSION

Above we have shown that it is possible to measure the kinetics for sublimation of graphite NPs, and for their oxidation by O_2. Obviously, what is needed to complete the story is information regarding the NP temperatures. Ultimately, it should be possible to obtain the temperature directly by modeling the intensity and wavelength dependence of the IR emission from hot NPs; however, for carbon, this would require detectors with sensitivity further into the near- or mid-IR. Because we are currently limited to wavelengths below 1100 nm, we are not able to derive temperatures from the emission spectra; however, it is useful to consider the factors that control the NP thermal balance, and to estimate limits on the NP temperatures and laser absorption cross sections.

A. Consider Sublimation. The NP temperature is determined by the balance between laser heating and cooling by collisions with the Ar buffer gas, by radiation, and by sublimation. In previous work with CdSe/ZnS quantum dots, where absorption cross sections could be estimated, we were able to develop a model for both the laser heating process and the various cooling processes.[5] In the case of the carbon NPs, we do not know the absorption cross sections at 532 nm, 445 nm, or 10.6 μm. Therefore, for the purposes of discussion, we take a different approach.

We start with the assumption that the sublimation rate per unit surface area for our graphite NPs is similar to that for polycrystalline graphite, and that the graphite NPs have surface areas equivalent to those of spherical particles of the same mass with the bulk graphite density. With these assumptions, we can use the measured mass loss rate to estimate the sublimation rate per unit area for each NP and then, by comparison to the known sublimation rates vs temperature for polycrystalline graphite, estimate the NP temperature. The assumed spherical NP shape gives a lower limit on the true NP surface areas. In addition, it is likely that the bulk graphite sublimation rate is also a lower limit on that for NPs, because the milled NPs almost certainly have a higher density of surface defect sites, which should have faster sublimation kinetics because they are less stable than perfect basal plane sites. The NP temperatures derived from these assumptions are, therefore, upper limits on the true temperatures. Note, however, that, because sublimation

kinetics are exponential in temperature, even large (e.g., factor of 5) underestimates of the (surface area × sublimation rate/area) product cause only modest (~5%) overestimation of the temperature.

The sublimation of graphite has been well studied due to its importance as a high temperature material. There are numerous studies of the vapor pressure vs temperature, as well as the ratio of various C_n species in the vapor phase.[21,23,26,27] There is a complex dependence of speciation on temperature, and there is also evidence that the sticking/accommodation coefficients for the various C_n are below unity. Fortunately, for our purposes, it suffices to know the rate vs temperature for sublimation of graphite into a vacuum, which has been measured in the 2350–2550 K range.[43,44] Furthermore, the measured sublimation rates are in reasonable agreement with models based on vapor pressure data,[44] which are available over a much wider temperature range. Table 1 summarizes the analysis of the mass loss rates in Figures 1 and 2, and gives the NP temperatures extracted by this method, which are in the 1700–2000 K range.

Next, we consider the cooling mechanisms, starting with evaporative cooling. Graphite sublimation is complicated by the fact that a distribution of C_n species desorbs; however, we can estimate an upper limit on evaporative cooling if we assume that only C atoms desorb. Using $\Delta H_{sub}(C) = 7.4$ eV/atom,[21] the fastest mass loss rate (1.65 MDa/min) gives a sublimation cooling power of ~3×10^{-15} W, which turns out to be insignificant compared to the other cooling mechanisms. Therefore, we do not consider evaporative cooling further. For the same reason, it is possible to ignore heating of the NPs by the oxidation reactions occurring when they are trapped in O_2, at least for the relatively low temperature range probed here.

B. Another Cooling Process Is Radiation. As discussed above, in the 500–1100 nm APD sensitivity range, the dominant emission appears to result from laser-excited PL of excitonic or surface states, although there is clearly also up-conversion of thermal energy to drive emission from these same states (Figure 6). From the photon count rate, corrected for the APD detection sensitivity, collection solid angle, and reflection losses in the optics, we can estimate the photon emission rate from the NPs, in the 500–1100 nm range. From the emission spectra, we can estimate that the energy-weighted average photon energy is ~1.5 eV, making it straightforward to estimate that cooling by this mechanism can carry away up to ~6×10^{-13} W, i.e., much more than evaporative cooling under these conditions.

Cooling by collisions with the Ar buffer gas is also important, particularly at higher pressures. The flux-weighted energy transfer per Ar-NP collision is $2k(T_{surface} - T_{gas}) \cdot c_A$, where $T_{surface}$ is the NP surface temperature, T_{gas} is the Ar temperature (~300 K), and c_A is the accommodation coefficient, which is a measure of the inelasticity of the collision. To calculate the collision rate, we used the surface area of the equivalent spherical particle of bulk graphite density; i.e., the estimated collisional cooling rates are lower limits. On the basis of scattering measurements of Ar from organic surfaces,[45,46] c_A is expected to be near unity for collisions between graphite and 300 K argon. For the small NP pumped at 532 nm in 3 mTorr of Ar, the collisional cooling powers are just under 10^{-12} W, while, for the larger NP pumped at 10.6 μm in 1 mTorr of Ar, the collisional cooling power is just above 10^{-12} W. For both particles, collisional cooling is significantly more important than

Table 1. Thermal Analysis of Figures 4 and 5

particle	pump laser intensity (W/cm²)	mass loss (Da/min)	avg. mass (Mda)	carbon atom loss rate (C/nm²/s)	T (K)	sublimation cooling (W)	radiative cooling 500–1100 nm (W)	P Ar (mTorr)	collisional cooling (W)	thermal radiative cooling (W)	total cooling rate (W)	$\sigma_{absorption}$ (cm²)	$\sigma_{geometric}$ (cm²)
Figure 1	46	362	14.7	2.09×10^{-4}	1700	6.0×10^{-19}	9.6×10^{-14}	3	9.0×10^{-13}	4.6×10^{-12}	5.6×10^{-12}	1.2×10^{-13}	7.7×10^{-12}
27.5 nm	100	978	14.6	5.67×10^{-4}	1734	1.6×10^{-18}	2.5×10^{-13}	3	9.1×10^{-13}	5.0×10^{-12}	6.2×10^{-12}	6.2×10^{-14}	7.6×10^{-12}
initial dia.	127	9100	14.4	5.33×10^{-3}	1816	1.5×10^{-17}	3.8×10^{-13}	3	9.5×10^{-13}	6.3×10^{-12}	7.6×10^{-12}	6.0×10^{-14}	7.6×10^{-12}
	146	53700	13.8	3.23×10^{-2}	1887	8.8×10^{-17}	5.6×10^{-13}	3	9.7×10^{-13}	7.4×10^{-12}	9.0×10^{-12}	6.1×10^{-14}	7.3×10^{-12}
	165	62000	13.2	3.85×10^{-2}	1895	1.0×10^{-16}	5.7×10^{-13}	3	9.5×10^{-13}	7.4×10^{-12}	8.9×10^{-12}	5.4×10^{-14}	7.1×10^{-12}
	73	609	12.9	3.83×10^{-4}	1720	1.0×10^{-18}	1.1×10^{-13}	3	8.3×10^{-13}	4.5×10^{-12}	5.4×10^{-12}	7.4×10^{-14}	7.0×10^{-12}
Figure 2	350	33600	94.5	5.61×10^{-3}	1818	5.5×10^{-17}	9.1×10^{-14}	1	1.1×10^{-12}	2.2×10^{-11}	2.3×10^{-11}	6.7×10^{-14}	2.6×10^{-11}
51.5 nm	530	293000	90.3	5.04×10^{-2}	1906	4.8×10^{-16}	1.7×10^{-13}	1	1.1×10^{-12}	2.7×10^{-11}	2.9×10^{-11}	5.4×10^{-14}	2.6×10^{-11}
initial dia.	700	1650000	85	2.96×10^{-1}	1984	2.7×10^{-15}	2.3×10^{-13}	1	1.2×10^{-12}	3.2×10^{-11}	3.3×10^{-11}	4.8×10^{-14}	2.5×10^{-11}

cooling from radiation in the 500−1100 nm range, except when pumping at high 532 nm intensities, where the two mechanisms are comparable.

The final cooling mechanism to be considered is blackbody-like thermal radiation. Unfortunately, most of the thermal radiation is expected to be at wavelengths longer than the 1100 nm cutoff of our Si APD. For example, at 1850 K, the peak of the blackbody emission spectrum is at 1566 nm, and the fraction of the total photon emission at wavelengths below 1100 nm is only ∼2.4%. Furthermore, most of those photons are in the near IR, where the APD quantum efficiency drops rapidly with increasing wavelength. If we take this factor into account, the fraction of the total thermal radiation that should be detectable by the APD is only ∼0.02%, and if we also account for the efficiency of our light collection optics, we can estimate that only ∼2 × 10^{-6} of the thermal photons are detected.

To estimate the cooling by thermal radiation, we used the Stephan Boltzmann law: $P \ (W/m^2) = \sigma \cdot \epsilon \cdot (T_{surface}^4 - T_{wall}^4)$, where σ is the Stephan Boltzmann constant and ϵ is the emissivity. T_{wall}, the trap electrode temperature, is near 300 K and has a negligible effect on the radiation balance. Again, we assumed spherical NPs; thus, the estimated cooling rate will be a lower limit. For ideal black bodies, $\epsilon = 1$, however, the emissivity of subwavelength NPs has been shown to be well below unity.[30,47−50] For NP diameters much less than λ, i.e., the case here, Mie theory predicts that emissivity should scale like λ^{-1},[30] i.e., proportional to the photon energy. This behavior was confirmed by Landstrom et al. for graphite and Fe/graphite core/shell particles in the 10−20 nm size range.[47] Taking $\epsilon(\lambda)$ measured by Landstrom et al. in the visible (∼0.065 at 400 nm, ∼0.035 at 700 nm) and applying λ^{-1} scaling to extrapolate ϵ into the infrared, we can estimate the thermal radiative cooling. For the smaller NP pumped at 532 nm, the thermal radiative cooling power is in the $(4.5−7.5) \times 10^{-12}$ W range, and for the larger NP pumped at 10.6 μm, the cooling power is in the $(1.3−3.3) \times 10^{-11}$ W range, reflecting the larger surface area. Thermal radiation, thus, accounts for between 81 and 96% of the total cooling under the pressure and temperature conditions of these experiments.

Because the laser heating power must equal the total cooling power at steady state, we can use the cooling powers and laser intensities to estimate the absorption cross section at 532 nm and 10.6 μm. The final two columns of the table compare the estimated absorption cross sections with the geometric cross sectional area of the NPs (assuming spherical shape). The geometric cross sections decline slightly during the experiments, reflecting the mass losses. We might expect that the absorption cross sections, which reflect either electronic or vibrational properties of the NPs, to be roughly independent of laser intensity, and the results of the thermal analysis are consistent with that expectation, within the uncertainties of the analysis. Most of the 532 nm cross sections are in the 6×10^{-14} cm^2 range, i.e., about 0.8% of the geometric cross section. The 10.6 μm cross sections average ∼5.6×10^{-14}, which is only ∼0.2% of the geometric cross section for the larger NP of that experiment. As noted above, the interaction of small NPs with light should vary like λ^{-1}; thus, it is not surprising that $\sigma_{absorption}/\sigma_{geometric}$ is smaller for 10.6 μm pumping. The outliers in the cross sections are the points for low 532 nm laser intensity, where the analysis suggests a larger absorption cross section. Note, however, that these points had very low mass loss rates, leading to greater uncertainties in both the mass loss measurement and the NP temperature estimates.

The results in Figure 7 provide some insight into these issues. In this experiment, the total photon count rate was measured for pump laser intensities of 41 and 57 W/cm^2 at 532 nm and 100 W/cm^2 at 10.6 μm, i.e., at the low end of the intensity ranges explored in Table 1. Recall that the APD-detectable emission appears to result from a combination of excitonic/surface state emission in the visible and near IR, and the high energy tail of the thermal emission spectrum in the IR, detected with low efficiency. Figure 6 shows that heating the NPs with 10.6 μm radiation results in emission that is quite similar to that from visible laser pumping, indicating that it is possible to populate the same set of excitonic and surface states thermally. Therefore, we expect the emission intensity to increase at higher NP temperatures, regardless of the excitation wavelength. The observation that emission is weakly pressure dependent at intermediate pressures is consistent with the prediction (Table 1) that thermal radiation should be the dominant cooling mechanism at low pressures, thus resulting in a weak dependence of NP temperature on Ar pressure. At pressures above ∼5 mTorr, however, collisional cooling starts to make a major contribution, and becomes the most important cooling mechanism above ∼20 mTorr under these conditions. As a result, the NP temperature drops, leading to a reduction in emission. At the lowest pressures, there appears to be a modest increase in the emission, presumably reflecting the elimination of collisional cooling, resulting in a small increase in temperature.

V. CONCLUSIONS

We have shown that thermally excited radiation is sufficient for detection and mass analysis of single trapped carbon NPs, even at the relatively low temperatures at which carbon NPs have near-zero sublimation rates. A model of the heating and cooling processes that determine the NP temperatures, and the associated sublimation rates, shows that thermal radiation and buffer gas collisions are the dominant cooling mechanisms over a wide range of conditions, including those for the rapid heating in Figure 5.

For carbon in the temperature range below 2000 K, it was impossible to extract temperatures from the emission spectra because only a weak tail of the thermal (blackbody-like) spectrum extends into the near-IR range detectable by our APD, and in addition, the analysis is complicated by strong emission at 750 nm from discrete electronic states. Use of mid-IR detectors would solve this problem, and allow quantitative temperature determination under reaction conditions. Note, however, that, for more refractory materials such as metal oxides, borides, or carbides, the temperature ranges of interest are above 3000 K; thus, the thermal radiation spectra should be far more intense ($I \propto T^4$) and shifted into the APD-detectable range. As a result, the detectable intensity of blackbody-like thermal radiation at wavelengths below 1100 nm would increase by more than an order of magnitude, and it would be possible to detect the spectral peak (∼966 nm at 3000 K), which provides a simple measure of the temperature.

■ ASSOCIATED CONTENT

Ⓢ Supporting Information

The Supporting Information is available free of charge on the ACS Publications website at DOI: 10.1021/acs.jpca.5b08499.

SEM images of graphite NPs (Figure S1), uncorrected NP ensemble emission spectra (Figure S2), and comparison of all the emission spectra (Figure S3) (PDF)

■ AUTHOR INFORMATION

Corresponding Author

*Phone: (+1) 801 585-7289. E-mail: anderson@chem.utah.edu.

Notes

The authors declare no competing financial interest.

■ ACKNOWLEDGMENTS

■ REFERENCES

(1) Fahrenholtz, W. G.; Wuchina, E. J.; Lee, W. E.; Zhou, Y. *Ultra-High Temperature Ceramics: Materials for Extreme Environment Applications*; John Wiley and Sons: Hoboken, NJ, 2014; p 456.

(2) Bell, D. M.; Howder, C. R.; Johnson, R. C.; Anderson, S. L. Single CdSe/ZnS Nanocrystals in an Ion Trap: Charge and Mass Determination and Photophysics Evolution with Changing Mass, Charge, and Temperature. *ACS Nano* **2014**, *8*, 2387−2398.

(3) Howder, C. R.; Bell, D. M.; Anderson, S. L. Optically Detected, Single Nanoparticle Mass Spectrometer with Pre-Filtered Electrospray Nanoparticle Source. *Rev. Sci. Instrum.* **2014**, *85*, 014104−014110.

(4) Howder, C. R.; Long, B. A.; Bell, D. M.; Anderson, S. L. Thermally Brightened CdSe/ZnS Quantum Dots as Non-Contact Probes for Surface Chemistry Studies of Dark Nanoparticles Trapped in the Gas Phase. *J. Phys. Chem. C* **2015**, *119*, 14561−14570.

(5) Howder, C. R.; Long, B. A.; Bell, D. M.; Furakawa, K. H.; Johnson, R. C.; Anderson, S. L. Photoluminescence of Charged CdSe/ZnS Quantum Dots in the Gas Phase: Effects of Charge and Heating on the Absorption and Emission Probabilities. *ACS Nano* **2014**, *8*, 12534−12548.

(6) Schulz, C.; Kock, B. F.; Hofmann, M.; Michelsen, H.; Will, S.; Bougie, B.; Suntz, R.; Smallwood, G. Laser-Induced Incandescence: Recent Trends and Current Questions. *Appl. Phys. B: Lasers Opt.* **2006**, *83*, 333−345.

(7) Nienow, A. M.; Roberts, J. T.; Zachariah, M. R. Surface Chemistry of Nanometer-Sized Aerosol Particles: Reactions of Molecular Oxygen with 30 Nm Soot Particles as a Function of Oxygen Partial Pressure. *J. Phys. Chem. B* **2005**, *109*, 5561−5568.

(8) Hars, G.; Tass, Z. Application of Quadrupole Ion Trap for the Accurate Mass Determination of Submicron Size Charged Particles. *J. Appl. Phys.* **1995**, *77*, 4245−50.

(9) Schlemmer, S.; Illemann, J.; Wellert, S.; Gerlich, D. Laboratory Experiments for the Investigation of Interstellar Dust Analogues. In *The Physics and Chemistry of the Interstellar Medium, Proceedings of the 3rd Cologne-Zermatt Symposium*; Ossenkopf, V., Stutzki, J., Winnewisser, G., Eds.; GCA-Verlag Herdecke: Aachen, Germany, 1999; pp 391−394.

(10) Schlemmer, S.; Illemann, J.; Wellert, S.; Gerlich, D. Nondestructive High-Resolution and Absolute Mass Determination of Single Charged Particles in a Three-Dimensional Quadrupole Trap. *J. Appl. Phys.* **2001**, *90*, 5410−5418.

(11) Schlemmer, S.; Wellert, S.; Windisch, F.; Grimm, M.; Barth, S.; Gerlich, D. Interaction of Electrons and Molecules with a Single Trapped Nanoparticle. *Appl. Phys. A: Mater. Sci. Process.* **2004**, *78*, 629−636.

(12) Grimm, M.; Langer, B.; Schlemmer, S.; Lischke, T.; Becker, U.; Widdra, W.; Gerlich, D.; Flesch, R.; Ruehl, E. Charging Mechanisms of Trapped Element-Selectively Excited Nanoparticles Exposed to Soft X Rays. *Phys. Rev. Lett.* **2006**, *96*, 066801/1−066801/4.

(13) Cai, Y.; Peng, W. P.; Kuo, S. J.; Lee, Y. T.; Chang, H. C. Single-Particle Mass Spectrometry of Polystyrene Microspheres and Diamond Nanocrystals. *Anal. Chem.* **2002**, *74*, 232−238.

(14) Cai, Y.; Peng, W. P.; Kuo, S. J.; Sabu, S.; Han, C. C.; Chang, H. C. Optical Detection and Charge-State Analysis of MALDI-Generated Particles with Molecular Masses Larger Than 5 MDa. *Anal. Chem.* **2002**, *74*, 4434−4440.

(15) Cai, Y.; Peng, W. P.; Chang, H. C. Ion Trap Mass Spectrometry of Fluorescently Labeled Nanoparticles. *Anal. Chem.* **2003**, *75*, 1805−1811.

(16) Peng, W. P.; Cai, Y.; Lee, Y. T.; Chang, H. C. Laser-Induced Fluorescence/Ion Trap as a Detector for Mass Spectrometric Analysis of Nanoparticles. *Int. J. Mass Spectrom.* **2003**, *229*, 67−76.

(17) Trevitt, A. J.; Wearne, P. J.; Bieske, E. J.; Schuder, M. D. Observation of Nondegenerate Cavity Modes for a Distorted Polystyrene Microsphere. *Opt. Lett.* **2006**, *31*, 2211−2213.

(18) Trevitt, A. J.; Wearne, P. J.; Bieske, E. J. Calibration of a Quadrupole Ion Trap for Particle Mass Spectrometry. *Int. J. Mass Spectrom.* **2007**, *262*, 241−246.

(19) Smith, T. A.; Trevitt, A. J.; Wearne, P. J.; Bieske, E. J.; McKimmie, L. J.; Bird, D. K. Morphology-Dependent Resonance Emission from Individual Micron-Sized Particles. *Springer Ser. Fluoresc.* **2007**, *4*, 415−429.

(20) Trevitt, A. J.; Wearne, P. J.; Bieske, E. J. Coalescence of Levitated Polystyrene Microspheres. *J. Aerosol Sci.* **2009**, *40*, 431−438.

(21) Brewer, L.; Gilles, P. W.; Jenkins, F. A. The Vapor Pressure and Heat of Sublimation of Graphite. *J. Chem. Phys.* **1948**, *16*, 797−807.

(22) Cao, L.; Meziani, M. J.; Sahu, S.; Sun, Y.-P. Photoluminescence Properties of Graphene Versus Other Carbon Nanomaterials. *Acc. Chem. Res.* **2013**, *46*, 171−180.

(23) Drowart, J.; Burns, R. P.; DeMaria, G.; Inghram, M. G. Mass Spectrometric Study of Carbon Vapor. *J. Chem. Phys.* **1959**, *31*, 1131−1132.

(24) Georgakilas, V.; Perman, J. A.; Tucek, J.; Zboril, R. Broad Family of Carbon Nanoallotropes: Classification, Chemistry, and Applications of Fullerenes, Carbon Dots, Nanotubes, Graphene, Nanodiamonds, and Combined Superstructures. *Chem. Rev.* **2015**, *115*, 4744−4822.

(25) Lim, S. Y.; Shen, W.; Gao, Z. Carbon Quantum Dots and Their Applications. *Chem. Soc. Rev.* **2015**, *44*, 362−381.

(26) Pitzer, K. S.; Clementi, E. Large Molecules in Carbon Vapor. *J. Am. Chem. Soc.* **1959**, *81*, 4477−4485.

(27) Steele, W. C.; Bourgelas, F. N. Studies of Graphite Vaporization Using a Modulated Beam Mass Spectrometer, Technical Report Afml-Tr-72-222, Avsd-0048-73-Cr; Air Force Materials Laboratory, Air Force Systems Command: Wright-Patterson Air Force Base, OH, 1972.

(28) Gerlich, D.; Decker, S. Trapping Ions at High Temperatures: Thermal Decay of C_{60}^+. *Appl. Phys. B: Lasers Opt.* **2014**, *114*, 257−266.

(29) Roberts, F. S.; Anderson, S. L. Hollow Cathode Lamp with Integral, High Optical Efficiency Isolation Valve: A Modular Vuv Source. *Rev. Sci. Instrum.* **2013**, *84*, 126101.

(30) Bohren, C. F.; Huffman, D. R. *Absorption and Scattering of Light by Small Particles*; Wiley: New York, 1983.

(31) Murray, V. J.; Marshall, B. C.; Woodburn, P. J.; Minton, T. K. Inelastic and Reactive Scattering Dynamics of Hyperthermal O and O_2 on Hot Vitreous Carbon Surfaces. *J. Phys. Chem. C* **2015**, *119*, 14780−14796.

(32) Baláž, P.; Achimovičová, M.; Baláž, M.; Billik, P.; Cherkezova-Zheleva, Z.; Criado, J. M.; Delogu, F.; Dutková, E.; Gaffet, E.; Gotor, F. J.; Kumar, R.; Mitov, I.; Rojac, T.; Senna, M.; Streletskiik, A.; Wieczorek-Ciurowa, K. Hallmarks of Mechanochemistry: From Nanoparticles to Technology. *Chem. Soc. Rev.* **2013**, *42*, 7571−7637.

(33) Gutman, E. M. *Mechanochemistry of Materials*; Cambridge International Science Publishing: Cambridge, U.K., 1998.

(34) Suryanarayana, C. Mechanical Alloying and Milling. *Prog. Mater. Sci.* **2001**, *46*, 1−184.

(35) McMahon, B. W.; Yu, J.; Boatz, J. A.; Anderson, S. L. Rapid Aluminum Nanoparticle Production by Milling in NH_3 and CH_3NH_2 Atmospheres: An Experimental and Theoretical Study. *ACS Appl. Mater. Interfaces* **2015**, *7*, 16101−16116.

(36) Perez, J. P. L.; McMahon, B. W.; Yu, J.; Schneider, S.; Boatz, J. A.; Hawkins, T. W.; McCrary, P. D.; Flores, L. A.; Rogers, R. D.; Anderson, S. L. Boron Nanoparticles with High Hydrogen Loading: Mechanism for B−H Binding and Potential for Improved Combustibility and Specific Impulse. *ACS Appl. Mater. Interfaces* **2014**, *6*, 8513−8525.

(37) Eda, G.; Lin, Y.-Y.; Mattevi, C.; Yamaguchi, H.; Chen, H.-A.; Chen, I.-S.; Chen, C.-W.; Chhowalla, M. Blue Photoluminescence from Chemically Derived Graphene Oxide. *Adv. Mater.* **2010**, *22*, 505−509.

(38) Heitz, T.; Godet, C.; Bouree, J. E.; Drevillon, B.; Conde, J. P. Radiative and Nonradiative Recombination in Polymerlike a-C:H Films. *Phys. Rev. B: Condens. Matter Mater. Phys.* **1999**, *60*, 6045−6052.

(39) Luo, Z.; Vora, P. M.; Mele, E. J.; Johnson, A. T. C.; Kikkawaa, J. M. Photoluminescence and Band Gap Modulation in Graphene Oxide. *Appl. Phys. Lett.* **2009**, *94*, 111909/3.

(40) Sun, X.; Liu, Z.; Welsher, K.; Robinson, J. T.; Goodwin, A.; Zaric, S.; Dai, H. Nano-Graphene Oxide for Cellular Imaging and Drug Delivery. *Nano Res.* **2008**, *1*, 203−212.

(41) Wang, Y.; Hu, A. Carbon Quantum Dots: Synthesis, Properties and Applications. *J. Mater. Chem. C* **2014**, *2*, 6921−6939.

(42) Lim, S. Y.; Shen, W.; Gao, Z. Carbon Quantum Dots and Their Applications. *Chem. Soc. Rev.* **2015**, *44*, 362−381.

(43) Tsai, C. C.; Gabriel, T. A.; Haines, J. R.; Rasmussen, D. A. Graphite Sublimation Tests for Target Development for the Muon Collider/Neutrino Factory. *IEEE/NPSS Symposium on Fusion Engineering* **2005**, *21*, 377−379.

(44) Haines, J. R.; Tsai, C. C. *Graphite Sublimation Tests for the Muon Collider/Neutrino Factory Target Development Program*; Oak Ridge National Laboratory: 2002; 6 pages.

(45) Alexander, W. A.; Zhang, J.; Murray, V. J.; Nathanson, G. M.; Minton, T. K. Kinematics and Dynamics of Atomic-Beam Scattering on Liquid and Self-Assembled Monolayer Surfaces. *Faraday Discuss.* **2012**, *157*, 355−374.

(46) King, M. E.; Nathanson, G. M.; Hanning-Lee, M. A.; Minton, T. K. Probing the Microscopic Corrugation of Liquid Surfaces with Gas-Liquid Collisions. *Phys. Rev. Lett.* **1993**, *70*, 1026−1029.

(47) Landstrom, L.; Elihn, K.; Boman, M.; Granqvist, C. G.; Heszler, P. Analysis of Thermalrradiation Fromllaser-Heated Nanoparticles Formed by Laser-Induced Decomposition of Ferrocene. *Appl. Phys. A: Mater. Sci. Process.* **2005**, *81*, 827−833.

(48) Landstrom, L.; Heszler, P. Analysis of Blackbody-Like Radiation from Laser-Heated Gas-Phase Tungsten Nanoparticles. *J. Phys. Chem. B* **2004**, *108*, 6216−6221.

(49) Roura, P.; Costa, J. Radiative Thermal Emission from Silicon Nanoparticles: A Reversed Story from Quantum to Classical Theory. *Eur. J. Phys.* **2002**, *23*, 191−203.

(50) van de Hulsst, H. C. *Light Scattering by Small Particles*; Dover: New York, 1981.